Controlling Organic Semiconductor Self-Assembly through Cylindrical Nanoconfinement

Zhuoqing Li,[†,‡] Kathrin Sentker,[†] Manuel Brinker,[†] Milena Lippmann,[¶] Oliver H. Seeck,[¶] Andriy V. Kityk,[§] Benjamin Ocko,[‖] and Patrick Huber[*,†,‡]

† *Institute for Materials and X-ray Physics, Hamburg University of Technology, Denickestr. 15, 21073 Hamburg, Germany*

‡ *Centre for X-ray and Nano Science CXNS, Deutsches Elektronen-Synchrotron DESY, Notkestr. 85, 22607 Hamburg, Germany*

¶*Photon Science, Deutsches Elektronen-Synchrotron DESY, Notkestr. 85, 22607 Hamburg, Germany*

§*Faculty of Electrical Engineering, Czestochowa University of Technology, Al. Armii Krajowej 17, P-42-200 Czestochowa, Poland*

‖*National Synchrotron Light Source II, Brookhaven National Laboratory, Upton, NY 11973, USA*

E-mail: patrick.huber@tuhh.de

Abstract

Controlling the self-assembly of organic semiconductors at the nanoscale is critical for advancing high-performance electronic and photonic devices, yet remains challenging due to their intrinsic anisotropic crystallization and sensitivity to processing conditions. Here, we demonstrate that cylindrical nanoconfinement within anodic aluminum oxide membranes provides a versatile platform to precisely tune the molecular orientation and phase behavior of the prototypical organic semiconductor 2,7-dioctyl[1]benzothieno[3,2-b][1]benzothiophene (C8-BTBT-C8). Combining temperature-dependent high-resolution synchrotron X-ray scattering with optical birefringence measurements, we uncover that confinement geometries (pore diameters 25–180 nm) and surface chemistry govern the emergence of distinct smectic A textures, featuring molecular layers either parallel or perpendicular to the pore axis. The competition between axial and radial smectic layering is modulated by pore size, surface hydrophilicity, and thermal history, enabling reversible control over domain orientations and transitions between liquid crystalline and crystalline states. Notably, nanoconfinement stabilizes the smectic phase over an expanded temperature range compared to bulk, while inducing complex multi-domain configurations owing to geometric constraints and anchoring conditions. Our results elucidate fundamental mechanisms by which anisotropic nanoscale confinement directs the self-organization of highly conjugated organic molecules, with implications for optimizing directional charge transport and anisotropic optical responses in organic–inorganic hybrid nanoarchitectures. This study establishes nanoconfinement as a powerful strategy to engineer morphology and functional properties in organic semiconducting materials with nanoscale precision.

Keywords

Keywords:smectic liquid crystal, nanoporous material, X-ray scattering, optical birefringence.

Introduction

Organic semiconducting materials, especially those that can be dissolved in solvents, have shown great potential for application in organic electronics and sensors.[1,2] Often they are considered in thin-film geometry and a substantial understanding of the resulting crystalline and liquid-crystalline texture has been achieved for these geometries.[3] Embedding these molecules in nanoporous membranes or cylindrical channels provides the opportunity to carry-out fundamental studies on self-assembly of functional molecules in confined geometries.[4–14] The resulting composites are also interesting as potential electro-optical materials, where the porous solid provides mechanical robustness, whereas the soft filling adds novel meta-optical[7,8,15,16] or electronic properties.[13,17] Moreover, the anisotropic confinement provides means to achieve geometry-determined texture selection depending on the targeted function of the hybrid material,[18,19] a major challenge for high-performance electronic and photonic applications of organic crystals.

In this study we probe the molecular orientation of 2,7-dioctyl[1]benzothieno[3,2-b][1]-benzot -hiophen (C8-BTBT-C8; see Fig. 1) deposited in cylindrical nanopores (25-180 nm) of monolithic anodized aluminum oxide (AAO) membranes. Temperature-dependent, high-resolution optical polarimetry and synchrotron radiation-based X-ray scattering methods were employed. C8-BTBT-C8 is a particular interesting candidate for organic electronics, since the smectic configurations of this mesogen are determined by strongly overlapping π-π interactions, resulting in a particularly high charge carrier mobility[2] within the smectic layers, i.e. perpendicular to the layering direction. A textural control of this can be achieved in thin-film geometries by applying an alternating external field (e.g., electric or magnetic fields), by introducing nucleation sites or temperature gradients.[1,3,20–22]

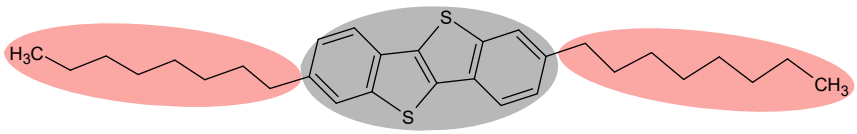

Figure 1: Chemical structure of 2,7-Dioctyl[1]benzothieno[3,2-b][1]benzothiophene (C8-BTBT-C8).

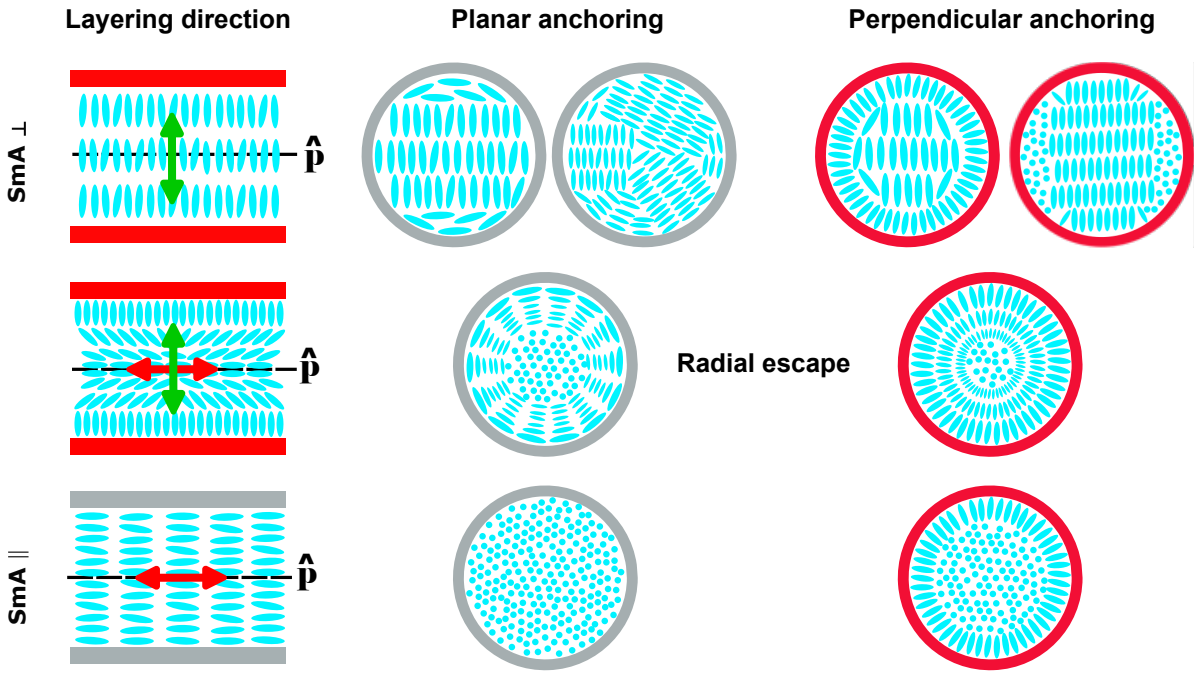

Figure 2: Crosssection and top view of possible smectic A textures in cylindrical nanoconfinement depending on mesogen wall anchoring. The smectic layering in radial (axial) direction is indicated by green (red) arrows with respect to the long pore axis direction $\hat{p}$.

Smectic layering in cylindrical confinement can adopt multiple configurations depending on the molecular anchoring at the pore walls. This anchoring can be chemically tuned by modifying the pore surfaces to be either hydrophobic or hydrophilic. Figure 2 illustrates possible textures arising from perpendicular or parallel anchoring at the pore interface.[23] Interestingly, in contrast to conventional rod-like liquid-crystalline systems, most prominently the cyanobiphenyl family - where hydrophilic surfaces typically induce planar anchoring - molecular dynamics simulations of this mesogen reveal the formation of a perpendicular layering configuration.[24] Notably, certain smectic arrangements within the pores facilitate cooperative intermolecular interactions, such as π–π stacking, which are crucial for achieving high charge-carrier transport properties.[2]

Here, we show that depending on the pore size, temperature and surface chemistry C8-BTBT-C8 can either adapt a molecular orientation with smectic layering direction (director $\hat{n}$) parallel or perpendicular to the long axis of cylindrical pores and in some conditions a mixture of these two orientations is also observed.

Results and discussion

Self-assembly of C8-BTBT-C8 in hydrophilic nanopores

We start the discussion with the smallest pore size, 25 nm diameter of the samples with hydrophilic pore surface. Upon cooling the isotropic melt to the liquid crystalline state, at a sample rotation angle $\omega = 90^{\circ}$ (incident beam perpendicular to the long pore axis direction $\hat{p}$), in the SAXS pattern we observe two Bragg peaks in the meridian directions with a wave vector transfer modulus of $q = (0.215 \pm 0.001)\,\text{Å}^{-1}$, see Fig. 3(a)(iii). They represent the (-100) and (100) smectic layer Bragg peaks Refs. ,[25] indicating layering parallel to the long pore axis $\hat{p}$ (axial layering). Upon further cooling to the crystalline phase, additional higher-order reflections at q =0.430 Å^{-1} and 0.646 Å^{-1} in the meridian direction are found in the WAXS pattenr, see Fig. 3(a)(ii), corresponding to the (200) and (300) Bragg peaks typical of layering in the crystalline phase (see Fig. 3(a)(ii)). We call these high and low temperature orientational domains with layering parallel to the long axes of the pores $\text{LC}_{\parallel}$ and $\text{Cry}_{\parallel}$ domains, respectively.

This texture evolution as a function of temperature is also corroborated by optical polarimetry measurements (see Fig. 3(a)(iv)). The optical retardation $R(T)$ rises quite abruptly to large positive values at $T = 410$ K upon cooling from the isotropic phase, indicating the isotropic-to-smectic phase transition with an alignment of the long molecular axes parallel to the long cylindrical axes of the pores. This observation aligns with the axial smectic layering condition extracted from the XRD patterns. Upon further cooling, there is a slight decrease in $R(T)$, even when the X-ray scattering experiment indicates a LC-to-crystalline phase transition. This is not unexpected, as the alignment of the molecules remains constant during such a phase transition. However, a slight decrease in the optical retardation value could suggest the formation of a small domain of molecules with radial (perpendicular to the pore axis) orientation. This domain disappears upon heating, accompanied by hysteresis, and subsequently, the collective orientational order is lost at the smectic-to-isotropic transition, exhibiting a hysteresis of a few degrees between heating and cooling.

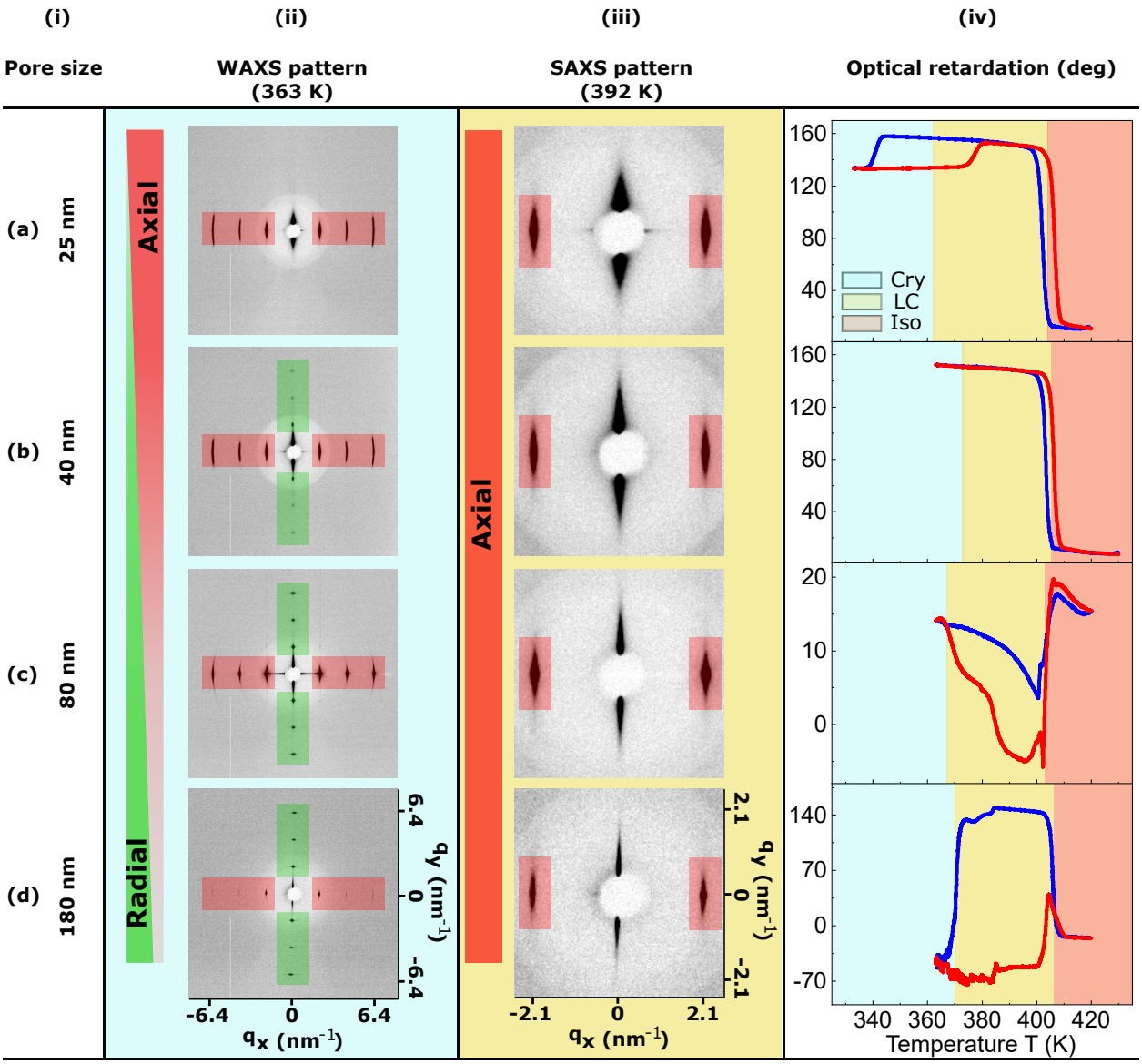

Figure 3: Self-assembly of C8-BTBT-C8 in hydrophilic cylindrical nanopores of different pore sizes in crystalline (blue background, (ii)), liquid crystalline (yellow background, (iii)) and isotropic (red background in (iv)) phases. The corresponding diffractograms in the columns (ii)&(iii) are measured at rotation angle $\omega = 90°$. All X-ray measurements are performed with a cooling/heating rate of 1 K/min. Column (iv) contains the corresponding temperature-dependent optical polarimetry measurements, blue/red curve is for cooling/heating.

For all hydrophilic pores larger than 25 nm the liquid crystalline state is still entirely dominated by an axial layering parallel to the pore axis, as indicated by smectic Bragg peaks in the meridian direction, see Fig. 3 panel (iii). However, upon cooling to the crystalline phase an additional contribution of a radial layering, perpendicular to $\hat{p}$ emerges, as indicated by the appearance of a sequence of layering peaks in the equatorial direction (q =0.215 Å^{-1}, 0.430 Å^{-1} and 0.646 Å^{-1}). They represent the (100), (200) and (300) crystal planes, respectively, see Fig. 3 panel (ii). Thus, in the larger pores, as a function of cooling a textural transition occurs from solely axial domains to domains with radial layering directions and this texture contribution increases with increasing pore size, a finding is based on the relative peak intensities for the peaks along the meridian and equitorial directions shown in Fig. 3 panel (ii). This development culminates for the largest pore size in a domain structure, where the meridian layering peaks have almost vanished. The structure is almost entirely dominated by a radial molecular layering.

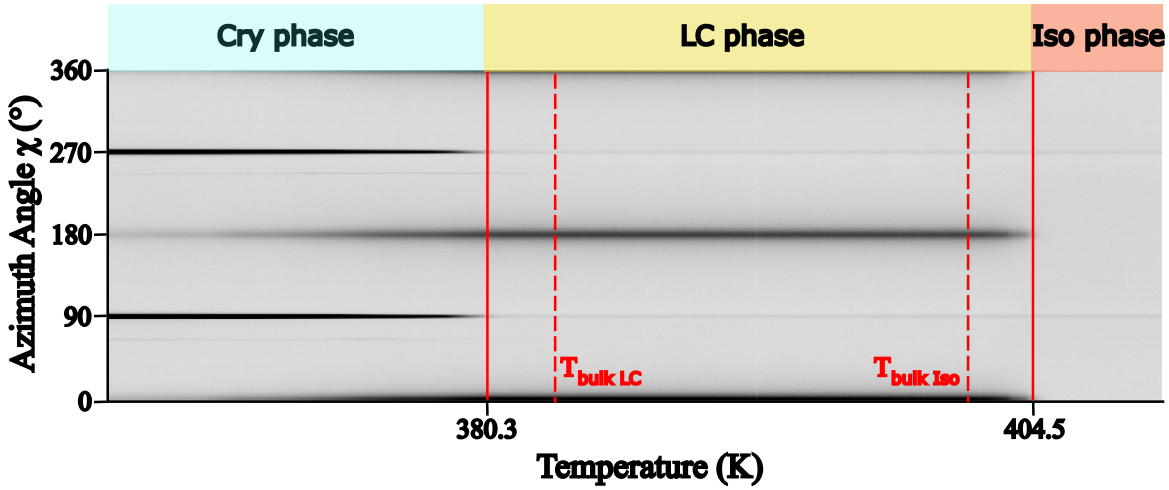

Figure 4: Evolution of the diffraction profiles with the temperature illustrating the transition from axial to radial smectic layering in 180 nm hydrophilic pores. Cooling with a rate of 1 K/min, progressing from the isotropic (Iso), through the liquid crystalline (LC), into the crystalline (Cry) phase.

To further illustrate the structural transition, the diffractograms of C8-BTBT-C8 confined in 180 nm hydrophilic nanopores are plotted as a function of temperature in Fig. 4. At low temperatures, in the Cry phase, four distinct diffraction peaks are observed at 0°/360°, 90°, 180° and 270°. Notably, the equatorial peaks at 90° and 270° are significantly stronger, indicating dominant radial domains.

As the temperature increases, the intensity of the equatorial peaks gradually decreases, while the peaks in the meridian direction (axial domains) at 0°/360° and 180° emerge. Between 360 K and 380 K, a clear coexistence of these two differently oriented domains is observed. Above 380 K, the equatorial peaks almost disappear, leaving only a weak signal at 90° and 270° coming from the membrane reflection. The meridional peaks signal a transition to a purely axial structure in the smectic liquid crystalline phase. Further heating above 397 K results in the complete transition to an isotropic phase. In this case, the equatorial peaks observed in the crystalline phase can be attributed either to logpile domains, in which the smectic layers grows across the pore diameter, or to radial domains, where the smectic layers form concentric rings. Both configurations satisfy the planar anchoring condition in hydrophilic pores and give rise to indistinguishable diffraction peaks along the equatorial direction.

The emergence of a radial orientation of the long axis of the molecules is also indicated by the optical polarimetry measurements. This is most evident for the 180 nm pores, where this textural transition is indicated by an abrupt drop in retardation to negative values upon cooling to the crystalline state, see Fig. 3(d)(iv). Interestingly, the system remains in this configuration upon heating. A few degree C below the smectic to isotropic transition an increasing axial contribution is indicated by an increase in retardation. While the 25 nm and 180 nm pore sizes are clear cases of a robust axial and radial, respectively, layering in the crystalline state, the diffraction and optical polarimetry data indicate rather mixed states for the intermediate pore sizes. This suggests that the energetic differences between axial and radial orientations must be relatively small, so that one or the other texture is present, depending on the history and subtleties of pore surface anchoring. Indeed, the approximately 10 times smaller optical retardation values in the case of the 80 nm channels, along with the nearly equal X-ray intensities along both directions, indicate an almost 50/50 distribution of axial and radial smectic layering.

Overall, the observation of radial layering is somewhat surprising. For such anisotropic channels as studied here, one would rather expect textures where the long axis of the molecules is aligned parallel to the long axis of the cylindrical pores.[26] Note, however, that similar counterintu-

itive textures have also been reported for lamellar crystals of rod-like n-alkanes[18] and n-alcohols[27] in tubular nanochannels of silicon. There, these peculiar orientations were attributed to textures determined by crystallization kinetics: The fast-growing crystal directions, i.e. the in-plane directions in which molecular backbones are placed side by side, are aligned parallel to the long channel axis (Bridgman growth). Presumably, this mechanism is also active here, favoring a collective rearrangement of the smectic stacks from axial to radial during crystallization. This also means that the planar anchoring strength for the C8-BTBT-C8 molecules is relatively low at the native AAO walls. In the 25 nm pores, the strong interfacial contribution is sufficient to suppress the Bridgman-growth-driven reorganization. For the larger pores it is already too weak and a collective rearrangement occurs during crystallization, which is also stable against heating to the liquid crystalline state. Interestingly, a similar observation has also been made for the smectic liquid crystal 12CB confined in 200 nm AAO channels.[28]

In Fig. 5 we show the coherence lengths of domains aligned either parallel ($\xi_{\parallel}$) or perpendicular ($\xi_{\perp}$) to the pore axis, measured across a range of pore sizes in both the crystalline and smectic phases. These values were extracted from XRD data using the Scherrer equation. In the smallest pores (25 nm), the cylindrical confinement appears to restrict the structure to axially aligned domains in both phases. For intermediate pore sizes (40 nm and 80 nm), the coherence lengths of the radial domains ($\xi_{\perp}$) exceed the half of the pore diameter, suggesting that lamellae may span the pore cross-section. In the largest pores (180 nm), however, $\xi_{\perp}$ is limited to approximately 60 nm. In this case, it remains uncertain whether the lamellae extend fully across the channels or form concentric ring-like structures. Considering the high curvature energy associated with the latter, a configuration in which lamellae traverse the pore is more likely. It is important to note that both XRD and optical measurements yield spatially averaged information and therefore do not permit detailed characterization of the distribution of axial and radial domains within individual pores. In particular, due to averaging over a large ensemble of channels, it remains unresolved whether different domain types coexist within a single pore or are distributed across different pores.

All of the diffractograms presented in Fig. 3(ii)&(iii) were obtained at a rotation angle ω of

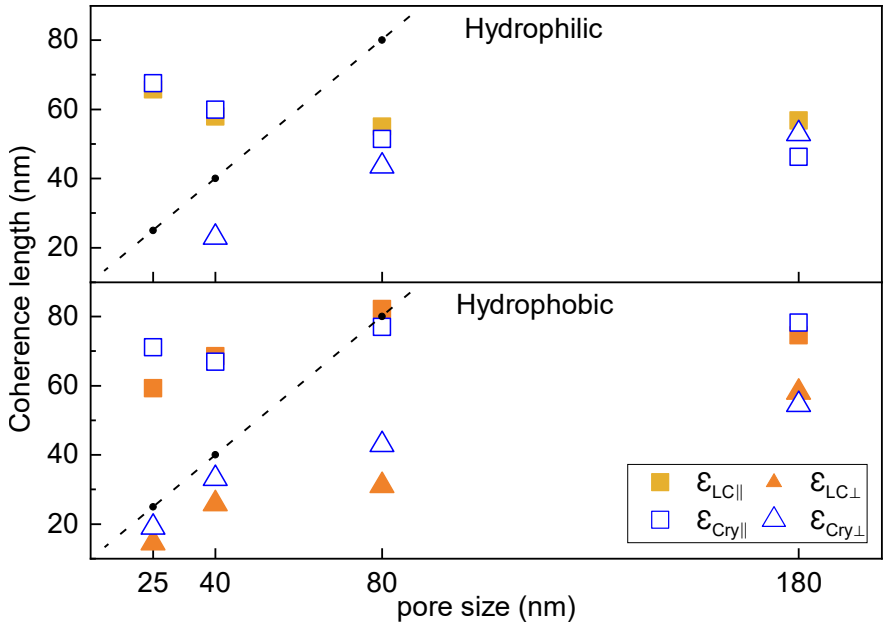

Figure 5: Coherence lengths parallel ($\xi_{\parallel}$) and perpendicular ($\xi_{\perp}$) to the long pore axis $\hat{p}$, measured in both the liquid-crystalline phase (at 392 K) and the crystalline phase (at 363 K), as a function of pore diameter (25, 40, 80, and 180 nm) and pore wall hydrophobicity. The dashed line represents the maximum possible value of $\xi_{\perp}$, corresponding to the pore diameter.

90°, which ensures that the incident X-ray beam is perpendicular to the direction of the pore axis $\hat{p}$. Fig. 6 shows typical results for the (a) axial/SmA$_{\parallel}$ and (b) planar radial/Cry$_{\perp}$ configuration a diffractogram at $\omega = 0°$, where the X-ray beam is parallel to $\hat{p}$. This configuration is only capable of probing translational order perpendicular to the direction of the incident X-ray beam. Therefore, no Bragg intensity is observed for the axial orientation. For the axial/SmA$_{\parallel}$ domains, smectic layering occurs exclusively in the direction parallel to the polarization vector. Conversely, the planar radial/Cry$_{\perp}$ configuration results in a diffraction ring that is powder-like in appearance, as illustrated in Fig. 6(b) at ω =0°. This ring is the result of the rotational averaging of the smectic peak intensity around the pore axis direction. As the rotation angle is increased, the ring disappears since the Bragg condition is no longer fulfilled. At approximately $\omega = 20°$ rotation, the Ewald sphere is bisected at two points on the meridian.

In contrast, for the axial configuration, the diffraction ring, for which the Bragg condition is not fulfilled at ω =0°, begins to intersect with the Ewald sphere on the equatorial line as late as $\omega = 80°$, see Fig. 6(a).

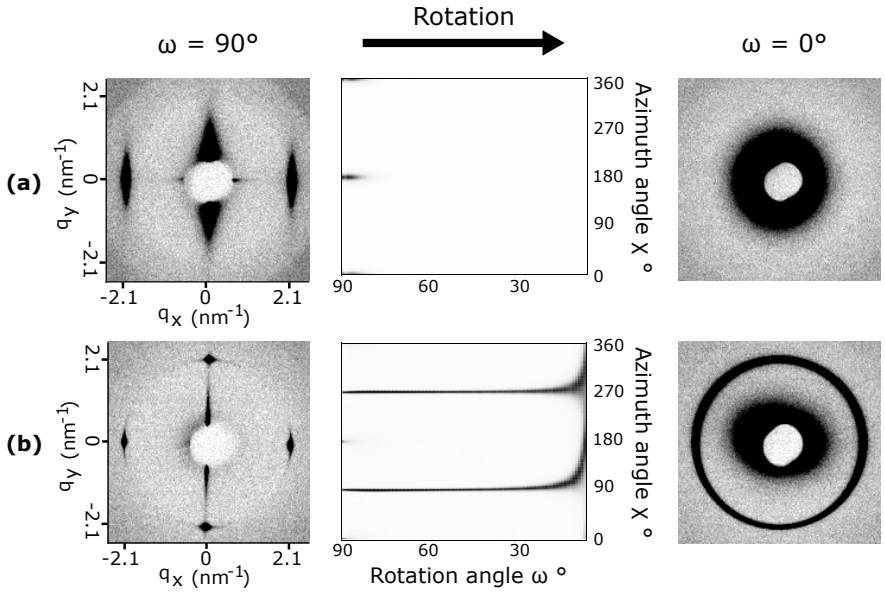

Figure 6: Typical diffractograms ($\omega = 90^\circ$ & 0°) and rotation scans for (a) pure axial alignment (d = 25 nm) and (b) planar logpile alignment (d = 180 nm) of the elongated molecules at 363 K in hydrophilic pores. The rotation scans show Bragg intensities for each azimuth (χ) angle extracted for each rotation angle ($\omega = 90^\circ \rightarrow 0^\circ$).

Self-assembly of C8-BTBT-C8 in hydrophobic nanopores

Fig. 7, panel (iii), presents the liquid crystalline X-ray diffractograms of C8-BTBT-C8 confined within hydrophobic nanopores. Upon cooling from the isotropic to the smectic phase, both meridional and equatorial reflections emerge at $q = (0.215 \pm 0.001)$,Å^{-1}, characteristic of smectic layering. As discussed above, the presence of meridional peaks indicates domains aligned parallel to the pore axis, while equatorial peaks correspond to domains oriented perpendicular to the axis. Further cooling into the crystalline phase leads to the appearance of higher-order reflections in both directions at $q = 0.430$ Å^{-1} and $q = 0.646$ Å^{-1}, corresponding to the (200) and (300) Bragg peaks typical of the crystalline structure (see Fig. 7, panel (ii)).

The texture evolution as a function of temperature is further investigated using optical polarimetry, as shown in Fig. 7, panel (iv). For small to intermediate pore sizes (25, 40, and 80 nm), the optical retardation curves exhibit a similar trend as with the x-ray results. A sharp decrease in retardation is first observed around 410 K, indicating an abrupt transition from the isotropic to the smectic phase. The transition is characterized by the emergence of predominantly radial

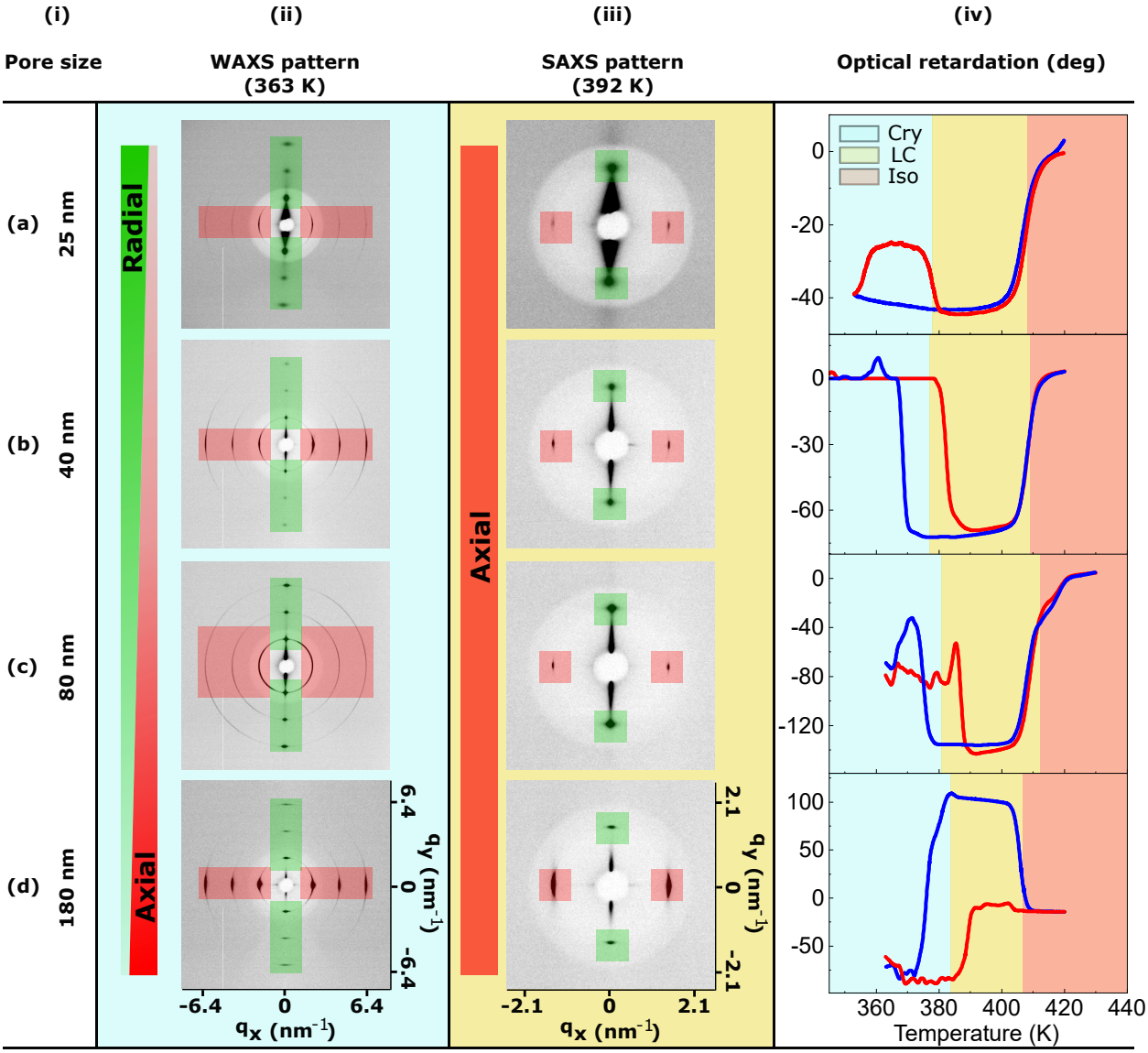

Figure 7: Self-assembly of C8-BTBT-C8 in hydrophobic cylindrical nanopores of different pore sizes in crystalline (blue background, (ii)), liquid crystalline (yellow background, (iii)) and isotropic (red background in (iV)) phases. The corresponding diffractograms in the columns (ii)&(iii) are measured at rotation angle $\omega = 90°$. All X-ray measurements are performed with a cooling/heating rate of 1 K/min. Column (iv) contains the corresponding temperature-dependent optical polarimetry measurements, blue/red curve is for cooling/heating.

domains—that is, domains oriented perpendicular to the pore axis. This observation is consistent with our X-ray scattering results: although both parallel and perpendicular domains coexist, the scattering intensity associated with the perpendicular domains is significantly stronger, suggesting that they constitute the dominant configuration within the nanopores. Upon further cooling into

the crystalline phase, the retardation values for small to intermediate pore sizes exhibit a clear increase accompanied by hysteresis. This suggests an enhanced contribution from the perpendicular domains in the crystalline state. In contrast, the optical retardation behavior observed for the largest pores (180 nm) shows the opposite trend. Upon cooling from the isotropic to the smectic phase, the retardation value increases (see Fig. 7(d)(iv)), indicating the dominance of axially aligned domains in the smectic phase. Further cooling into the crystalline phase results in a decrease in retardation, suggesting an increasing contribution from radial domains. This behavior is consistent with the X-ray scattering data, where meridional peaks—associated with perpendicular (radial) domains—exhibit higher intensity in the smectic phase.

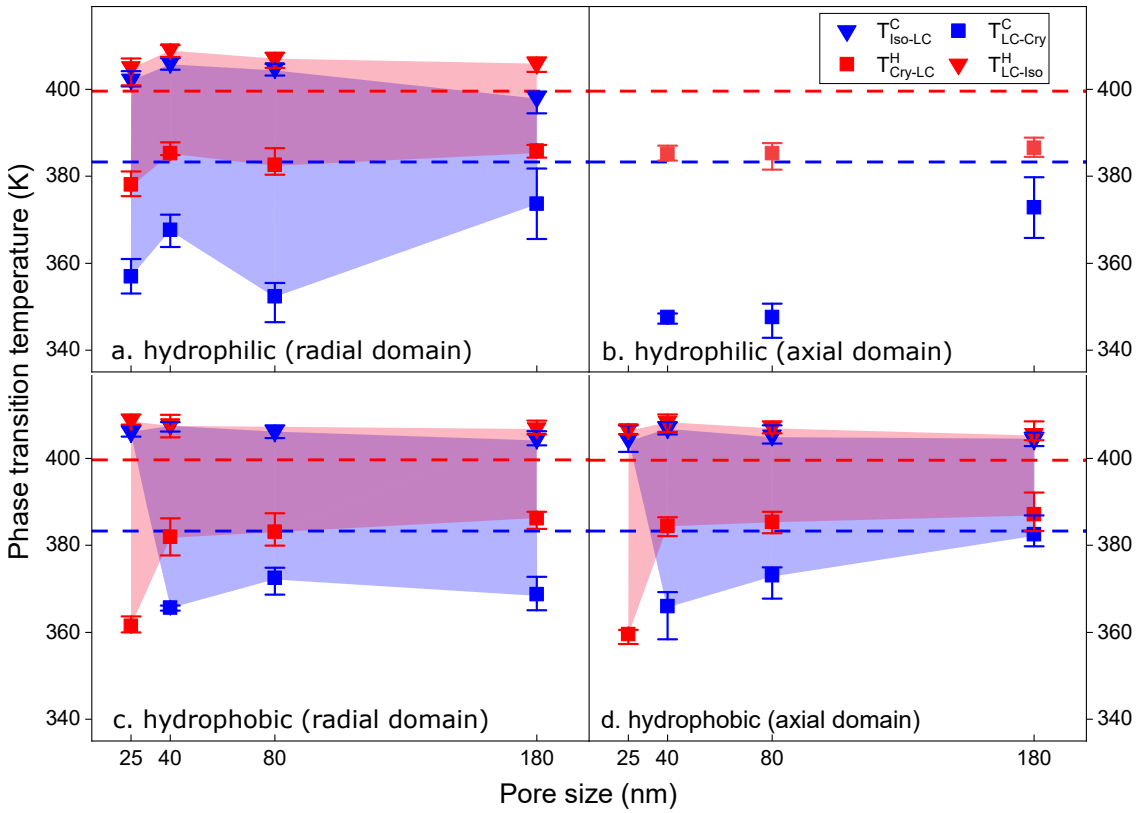

Figure 8: Phase transition temperatures of parallel (a & c) and perpendicular (b & d) domain orientations confined within hydrophilic and hydrophobic pores extracted from XRD measurements. The transition temperatures from the LC to Cry phase (T_{LC-Cry}) and from the Iso to LC phase (T_{Iso-LC}) are shown upon cooling (T^{C}, blue) and heating (T^{H}, red) as a function of the pore diameter. Dashed lines indicate the corresponding bulk transition temperatures: T^{bulk}_{LC-Cry} (blue) and T^{bulk}_{Iso-LC} (red). The shaded regions represent the temperature ranges over which the LC phase is observed during both cooling and heating cycles.

In hydrophobic pores, both radial and axial domain orientations are observed. However, since the scattering data represent an average over a large number of pores, it is not possible to ascertain whether these domain types coexist within individual pores or are distributed across different pores. Nevertheless, the appearance of arc-like meridional peaks in the crystalline phase suggests the possibility of a radial escape configuration. In such a scenario, $SmA_{\perp}$ domains are located near the pore walls, while $SmA_{\parallel}$ domains, aligned along the pore axis, occupy the central region to minimize distortion. A smooth transition between the axial core and the radial periphery could account for the observed arc-shaped diffraction features. This hypothesis is supported by earlier work from Kralj and Žumer,[29] who studied the relative stability of smectic-A phases confined in cylindrical geometries. Their theoretical analysis showed that mixed radial escape configurations—featuring both axial and radial components—can be stabilized under conditions of strong homeotropic anchoring.

In Fig. 8 we summarize the phase transition behavior by a comparison of the transition temperatures in the confined state with the ones in the bulk, as inferred from the XRD measurements. They are denoted as T_{Iso-LC} and T_{LC-Cry} for domains oriented either parallel or perpendicular to the long pore axis, since they exhibit distinct freezing and melting temperatures. It should be noted that the perpendicular domain in the hydrophilic pores is observed only in the crystalline phase, as shown in Fig. 8b. Additionally, the T_{LC-Cry} value for the 25 nm pores during the cooling cycle in Fig. 8c & d is not available due to a beam dump that occurred during the synchrotron-based XRD measurement. The phase transition temperature T_{Iso-LC} for both parallel and perpendicular domain orientations remains largely unaffected across the range of pore sizes and in both hydrophilic and hydrophobic environments. Compared to the bulk state, the confined T_{Iso-LC} is, on average, approximately 4 K higher than the bulk transition temperature (399 K), with hardly any hysteresis between cooling and heating. This is not too surprising, as a significant lowering of liquid crystalline phase transitions has often been observed for pore sizes below 10 nm for mesogens of this size.[9] In fact, anisotropic confinement favors the low-temperature LC phase with respect to the collective orientational arrangement of the rods, particularly in the axial state,[4,9,30] which may

explain the slight increase in observed transition temperatures.

In contrast, the T_{LC-Cry} exhibits a pronounced hysteresis between the heating and cooling cycles. During the heating cycle, the T_{LC-Cry} remains nearly unchanged relative to the bulk phase transition temperature (383 K). However, during the cooling cycle, the T_{LC-Cry} is significantly lower than that of the bulk material. On average, in hydrophilic pores, the T_{LC-Cry} is approximately 20 K below the bulk transition temperature, while in hydrophobic pores it is reduced by about 10 K. As a result, in the cooling cycle the liquid crystalline phase range is much broader than its bulk state, see the shaded phase existence ranges in Fig. 8. Similar observations have been made regarding the crystallization of various molecular systems, ranging from simple van-der-Waals systems to long-chain hydrocarbons and polymers.[5,31–35] Unlike the liquid crystalline state, the formation of well-defined crystalline packing is often more hindered by the absence of suitable nucleation centers, as well as the additional defect energies required for the crystal to adapt to the confining geometry.[34]

Conclusion

In conclusion, our findings indicate that the orientational order of confined C8-BTBT-C8 is dependent on both pore diameter and surface functionality. In hydrophilic pores, a pure axial configuration is invariably the preferred arrangement in the LC phase, irrespective of pore size. However, upon entering the Cry phase, the confinement effect begins to exert influence over the molecular self-assembly. In smaller pores with a diameter of 25 nm, the extreme confinement leads to a preference for the axial configuration with minimal bend and splay distortion. In contrast, in larger pores (d = 180 nm), a radial configuration is observed to be dominant. Pore sizes between 40 and 80 nm exhibit a mixed molecular configuration, characterised by both axial and radial orientation, potentially also the continuous transition between radial to axial order in one pore, so-called radial escape structures. Conversely, in hydrophobic pores, a dominant central concentric ring structure is consistently observed in the LC phase across all pore sizes. Given the semiconducting properties of the C8-BTBT-C8 molecules, it is likely that the formation of a central concentric ring

structure may facilitate high charge carrier mobility along the pore direction. Upon cooling into the Cry phase, a mixture of axial and radial configurations is observed for all pore sizes. With an increase in pore size, the axial component becomes more pronounced.

Experimental

C8-BTBT-C8 was purchased from Sigma-Aldrich and filled into nanoporous AAO membranes via spontaneous imbibition[36] as described in Ref. [8] Bulk C8-BTBT-C8 shows a SmA phase between 383.3 K and 399.6 K and possesses a monoclinic unit cell resulting in a small angle (001) layering peak at $q_{(001)} = 0.219\,\text{Å}^{-1}$.[25]

The AAO membranes with four different pore diameters were purchased from SmartMembranes GmbH (SM). The pore diameters d are provided by the SmartMembranes company and porosities P are calculated from the pore diameter and pore pitch as $d = 25\,\text{nm}$ and $P = 13.4\,\%$, $d = 40\,\text{nm}$ and $P = 9.3\,\%$, $d = 80\,\text{nm}$ and $P = 37.1\,\%$ and $d = 180\,\text{nm}$ and $P = 12.7\,\%$. Naturally the AAO membrane surface is hydrophilic but can be made hydrophobic by grafting alkyl chains onto the pore walls through chemical treatment with octadecylphosphonic acid (ODPA) as described in the Refs. [37–39]

To obtain detailed information about the molecular packing of C8-BTBT-C8, temperature-dependent (1 K/min cooling and heating rate) X-ray diffraction (XRD) experiments in transmission were performed at the P08 beamline[40] of the PETRA III synchrotron at Deutsches Elektronen-Synchrotron DESY (beam size (VxH) = $(200\times200)\,\mu\text{m}^2$, beam wavelength $\lambda = 0.496\,\text{Å}$, Perkin Elmer detector) and at the 11-BM (CMS) beamline of the National Synchrotron Light Source II (NSLS II) (beam size (VxH) = $(200\times200)\,\mu\text{m}^2$, beam wavelength $\lambda = 0.7294\,\text{Å}$, pilatus 2M detector). The accessible q-range was in the tender small angle x-ray scattering (SAXS) regime and in the intermediate region towards the wide angel x-ray scattering (WAXS) region. The images in the tender SAXS regime are referred with SAXS and the images in intermediate region with WAXS respectively.

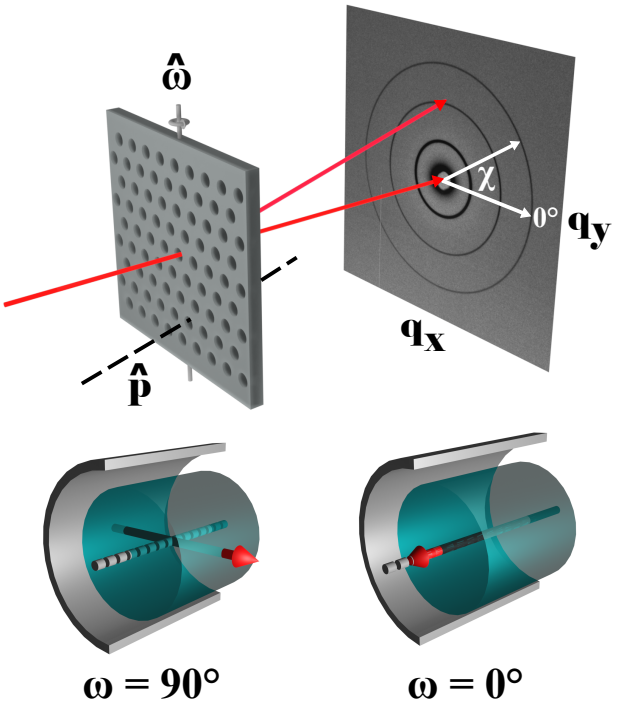

Figure 9: Schematics of the synchrotron-based X-ray scattering experiment and definition of azimuth angle χ and sample rotation angle ω for a configuration with incident X-ray beam parallel or perpendicular to the long cylindrical pore axis direction $\hat{p}$, respectively.

A sketch of the scattering geometry and used naming is presented in Fig. 9 for conventions. Following the nomenclature convention of fibre texture analysis, where the long nanopore axis $\hat{p}$ is identified with the fibre axis, the scattering patterns are described with respect to the equator (vertical axis) and meridian (horizontal axis), azimuth angle χ and sample rotation angle ω, see Fig. 9. Temperature-dependent X-ray scattering patterns are taken at ω =90°, where the X-ray beam is perpendicular to the long pore axis $\hat{p}$. Additional rotation scans are performed in the smectic phase and crystalline phase for sample rotation angles from $\omega = 90°$ to 0°. For $\omega =$ 90° only order in the plane defined by the equator and $\hat{p}$ is probed, while $\omega = 0°$ probes dominantly order in a plane perpendicular to $\hat{p}$ since the scattering vector $\vec{q}$ is nearly perpendicular to the beam direction at small scattering angles.

By performing Gaussian lineshape fits to the scattering profiles the full width at half maximum (FWHM) is extracted and in turn enables a calculation of the average domain sizes by using the Scherrer equation. Here, the domain size $\xi = K \cdot \lambda / \Delta\theta \cdot \cos(\theta)$ where λ is the X-ray wavelength,

θ is the Bragg angle, $\Delta\theta$ is the fit obtained FWHM and $K = 0.9$ is an empirical proportionality factor. Using this approach both the crystalline sizes $\xi_{\parallel}$ and $\xi_{\perp}$ parallel and perpendicular to the long pore axis direction $\hat{p}$ are determined, respectively.

Temperature-dependent (0.15 K/min cooling and heating rate) high-resolution optical polarimetry measurements, sensitive to the optical retardation $R(T)$ between perpendicularly polarized ordinary and extraordinary beams, complements the results obtained by X-ray scattering. The optical retardation is directly sensitive to the collective molecular orientational order, thereby offering a quantitative probe of the degree of orientational ordering in the system.[8,26]

Acknowledgement

Funding by the Deutsche Forschungsgemeinschaft (DFG, German Reserch Foundation) Projektnummer 192346071, SFB 986 "Tailor-Made Multi-Scale Materials Systems" Projektnummer 430146019, the DFG project "Ionic Liquid Crystals Confined in Nanoporous Solids: Self-Assembly, Molecular Mobility and Electro-Optical Functionalities" funding code HU 850/13-1, as well HU 850/5-1 is acknowledged. We thank Deutsche Elektronen-Synchrotron DESY, Hamburg for access to the beamline P08 of the PETRA III synchrotron. Moreover, we acknowledge experimental support from Masafumi Fukuto at the Complex Materials Scattering (CMS) beamline 11-BM of the National Synchrotron Light Source II (NSLS-II), a U.S. Department of Energy (DOE) Office of Science User Facility operated by Brookhaven National Laboratory under Contract No. DE-SC0012704. The presented results are part of a project that has received funding from the European Union Horizon Europe research and innovation programme under the Marie Skłodowska-Curie Grant agreement no.101086493. A.V.K. acknowledges the project cofinanced by the Polish Ministry of Education and Science under the program "Co-financed international projects", project no. W26/HE/2023 (Dec. MEiN 5451/HE/2023/2).

References

(1) Molina-Lopez, F.; Yan, H.; Gu, X.; Kim, Y.; Toney, M. F.; Bao, Z. Electric Field Tuning Molecular Packing and Electrical Properties of Solution-Shearing Coated Organic Semiconducting Thin Films. *Advanced Functional Materials* **2017**, *27*.

(2) Izawa, T.; Miyazaki, E.; Takimiya, K. Molecular ordering of high-performance soluble molecular semiconductors and re-evaluation of their field-effect transistor characteristics. *Advanced Materials* **2008**, *20*, 3388–3392.

(3) Hawly, T.; Johnson, M.; Späth, A.; Nickles Jäkel, H.; Wu, M.; Spiecker, E.; Watts, B.; Nefedov, A.; Fink, R. H. Exploring the Preparation Dependence of Crystalline 2D-Extended Ultrathin C8-BTBT-C8 Films. *ACS Applied Materials and Interfaces* **2022**, *14*, 16830–16838.

(4) Kityk, A. V.; Huber, P. Thermotropic nematic and smectic order in silica glass nanochannels RID B-7690-2008. *Applied Physics Letters* **2010**, *97*, 153124.

(5) Huber, P. Soft matter in hard confinement: phase transition thermodynamics, structure, texture, diffusion and flow in nanoporous media. *Journal of Physics: Condensed Matter* **2015**, *27*, 103102.

(6) Ryu, S. H.; Yoon, D. K. Liquid crystal phases in confined geometries. *Liquid Crystals* **2016**, *8292*, 1–22.

(7) Sentker, K.; Zantop, A. W.; Lippmann, M.; Hofmann, T.; Seeck, O. H.; Kityk, A. V.; Yildirim, A.; Schönhals, A.; Mazza, M. G.; Huber, P. Quantized Self-Assembly of Discotic Rings in a Liquid Crystal Confined in Nanopores. *Physical Review Letters* **2018**, *120*, 067801.

(8) Sentker, K.; Yildirim, A.; Lippmann, M.; Zantop, A. W.; Bertram, F.; Hofmann, T.; Seeck, O. H.; Kityk, A. V.; Mazza, M. G.; Schönhals, A.; Huber, P. Self-assembly of liquid crystals in nanoporous solids for adaptive photonic metamaterials. *Nanoscale* **2019**, *11*, 23304–23317.

(9) Gang, O.; Huber, P.; Karim, A.; Zvonkina, I.; Lee, S.-W.; Kim, J.-W.; Roper, D. K.; Li, W. J. *Soft Matter and Biomaterials on the Nanoscale*; World Scientific, 2020; Vol. 1.

(10) Monderkamp, P. A.; Wittmann, R.; Cortes, L. B.; Aarts, D. G.; Smallenburg, F.; Löwen, H. Topology of Orientational Defects in Confined Smectic Liquid Crystals. *Physical Review Letters* **2021**, *127*, 198001.

(11) Dietrich, C. F.; Rudquist, P.; Lorenz, K.; Giesselmann, F. Chiral structures from achiral micellar lyotropic liquid crystals under capillary confinement. *Langmuir* **2017**, *33*, 5852–5862.

(12) Kolmangadi, M. A.; Zhuoqing, L.; Smales, G. J.; Pauw, B. R.; Wuckert, E.; Raab, A.; Laschat, S.; Huber, P.; Schönhals, A. Confinement-Suppressed Phase Transition and Dynamic Self-Assembly of Ionic Superdiscs in Ordered Nanochannels: Implications for Nanoscale Applications. *ACS Applied Nano Materials* **2023**, *6*, 15673–15684.

(13) Li, Z.; Raab, A.; Kolmangadi, M. A.; Busch, M.; Grunwald, M.; Demel, F.; Bertram, F.; Kityk, A. V.; Schönhals, A.; Laschat, S.; Huber, P. Self-Assembly of Ionic Superdiscs in Nanopores. *ACS Nano* **2024**, *18*, 14414–14426, PMID: 38760015.

(14) Maksym, A. Z.; Andrushchak, A. S.; Shchur, Y.; Sahraoui, B.; Kula, P.; Lelonek, M.; Busch, M.; Huber, P.; Kityk, A. V. Self-Assembly of Bent-Core Nematics in Nanopores. *Small* **2025**, e06651.

(15) Kityk, A. V.; Nowak, M.; Reben, M.; Pawlik, P.; Lelonek, M.; Andrushchak, A.; Shchur, Y.; Andrushchak, N.; Huber, P. Dynamic Kerr and Pockels electro-optics of liquid crystals in nanopores for active photonic metamaterials. *Nanoscale* **2021**,

(16) Waszkowska, K.; Josse, P.; Cabanetos, C. C.; Blanchard, P.; Sahraoui, B.; Guichaoua, D.; Syvorotka, I.; Kityk, O.; Wielgosz, R.; Huber, P.; Kityk, A. V. Anisotropic confinement of chromophores induces second-order nonlinear optics in a nanoporous photonic metamaterial. *Optics Letters* **2021**, *46*, 845.

(17) Yildirim, A.; Sentker, K.; Smales, G. J.; Pauw, B. R.; Huber, P.; Schönhals, A. Collective orientational order and phase behavior of a discotic liquid crystal under nanoscale confinement. *Nanoscale Advances* **2019**, *1*, 1104–1116.

(18) Henschel, A.; Hofmann, T.; Huber, P.; Knorr, K. Preferred orientations and stability of medium length n-alkanes solidified in mesoporous silicon. *Phys. Rev. E* **2007**, *75*, 21607.

(19) Bisoyi, H. K.; Li, Q. Stimuli directed alignment of self-organized one-dimensional semiconducting columnar liquid crystal nanostructures for organic electronics. 2019.

(20) Dohr, M.; Ehmann, H. M. A.; Jones, A. O. F.; Salzmann, I.; Shen, Q.; Teichert, C.; Ruzié, C.; Schweicher, G.; Geerts, Y. H.; Resel, R.; Sferrazza, M.; Werzer, O. Reversibility of temperature driven discrete layer-by-layer formation of dioctyl-benzothieno-benzothiophene films. *Soft Matter* **2017**, *13*, 2322–2329.

(21) Jo, P. S.; Vailionis, A.; Park, Y. M.; Salleo, A. Scalable fabrication of strongly textured organic semiconductor micropatterns by capillary force lithography. *Advanced Materials* **2012**, *24*, 3269–3274.

(22) Schweicher, G.; Liu, G.; Fastré, P.; Resel, R.; Abbas, M.; Wantz, G.; Geerts, Y. H. Directional crystallization of C8-BTBT-C8 thin films in a temperature gradient. *Materials Chemistry Frontiers* **2021**, *5*, 249–258.

(23) Crawford, G. P.; Allender, D. W.; Doane, J. W. Surface elastic and molecular-anchoring properties of nematic liquid crystals confined to cylindrical cavities. *Physical Review A* **1992**, *45*, 8693–8708.

(24) Provenzano, S.; Casalegno, M. Characterization of thermal behavior and surface properties of C8-BTBT-C8 by means of molecular dynamics simulations. Master Thesis, Politecnico di Milano, Piazza Leonardo da Vinci, 32, 20133 Milano MI, Italy, 2021.

(25) Grigoriadis, C.; Niebel, C.; Ruzié, C.; Geerts, Y. H.; Floudas, G. Order, viscoelastic, and dielectric properties of symmetric and asymmetric alkyl[1]benzothieno[3,2-b][1]benzothiophenes. *Journal of Physical Chemistry B* **2014**, *118*, 1443–1451.

(26) Kityk, A. V.; Wolff, M.; Knorr, K.; Al., E.; Morineau, D.; Lefort, R.; Huber, P. Continuous paranematic-to-nematic ordering transitions of liquid crystals in tubular silica nanochannels. *Phys. Rev. Lett.* **2008**, *101*, 187801.

(27) Henschel, A.; Huber, P.; Knorr, K. Crystallization of medium-length 1-alcohols in mesoporous silicon: An x-ray diffraction study. *Physical Review E* **2008**, *77*, 42602.

(28) Chahine, G.; Kityk, A. V.; Demarest, N.; Jean, F.; Knorr, K.; Huber, P.; Lefort, R.; Zanotti, J.-M.; Morineau, D. Collective molecular reorientation of a calamitic liquid crystal (12CB) confined in alumina nanochannels. *Physical review. E, Statistical, nonlinear, and soft matter physics* **2010**, *82*, 11706.

(29) Kralj, S.; Žumer, S. Smectic-A structures in submicrometer cylindrical cavities. *Phys. Rev. E* **1996**, *54*, 1610–1617.

(30) Crawford, G. P., Zumber, S., Eds. *Liquid Crystals in Complex Geometries Formed by Polymer and Porous Networks*; Taylor and Francis; New York, U.S.A., 1996.

(31) Huber, P.; Knorr, K. Adsorption-desorption isotherms and x-ray diffraction of Ar condensed into a porous glass matrix. *Phys. Rev. B* **1999**, *60*, 12657.

(32) Alba-Simionesco, C.; Coasne, B.; Dosseh, G.; Dudziak, G.; Gubbins, K. E.; Radhakrishnan, R.; Sliwinska-Bartkowiak, M. Effects of confinement on freezing and melting. *J. Phys.: Condens. Matter* **2006**, *18*, R15.

(33) Schaefer, C.; Hofmann, T.; Wallacher, D.; Huber, P.; Knorr, K. Melting and freezing of argon in a granular packing of linear mesopore arrays. *Phys. Rev. Lett.* **2008**, *100*, 175701.

(34) Duran, H.; Steinhart, M.; Butt, H.-J. J.; Floudas, G. From Heterogeneous to Homogeneous Nucleation of Isotactic Poly(propylene) Confined to Nanoporous Alumina. *Nano Letters* **2011**, *11*, 1671–1675.

(35) Michell, R. M.; Blaszczyk-Lezak, I.; Mijangos, C.; Mueller, A. J. Confinement effects on polymer crystallization: From droplets to alumina nanopores. *Polymer* **2013**, *54*, 4059–4077.

(36) Gruener, S.; Huber, P. Imbibition in mesoporous silica: rheological concepts and experiments on water and a liquid crystal. *J. Phys.: Condens. Matter* **2011**, *23*, 184109.

(37) Klauk, H.; Zschieschang, U.; Pflaum, J.; Halik, M. Ultralow-power organic complementary circuits. *Nature* **2007**, *445*, 745–748.

(38) Grigoriadis, C.; Duran, H.; Steinhart, M.; Kappl, M.; Butt, H. J.; Floudas, G. Suppression of Phase Transitions in a Confined Rodlike Liquid Crystal. *Acs Nano* **2011**, *5*, 9208–9215.

(39) Khassanov, A.; Steinrück, H. G.; Schmaltz, T.; Magerl, A.; Halik, M. Structural investigations of self-assembled monolayers for organic electronics: Results from X-ray reflectivity. *Accounts of Chemical Research* **2015**, *48*, 1901–1908.

(40) Seeck, O. H.; Deiter, C.; Pflaum, K.; Bertam, F.; Beerlink, A.; Franz, H.; Horbach, J.; Schulte-Schrepping, H.; Murphy, B. M.; Greve, M.; Magnussen, O. The high-resolution diffraction beamline P08 at PETRA III. *Journal of Synchrotron Radiation* **2012**, *19*, 30–38.

TOC Graphic